Surface and Tethered-Balloon Observations of Actinic Flux: Effects of Arctic stratus, Surface Albedo and Solar Zenith Angle

Stephan R. de Roode, Peter G. Duynkerke, Wim Boot, and Jeroen C. H. Van der Hage

Institute for Marine and Atmospheric Research Utrecht (IMAU)

Utrecht University

The Netherlands

Submitted to the J. Geophys. Res., 9 July 2000

Correspondence to: S. R. de Roode, University of Washington, Dept of Atmospheric Sciences, Box 351640, Seattle, WA 98195-1640 USA. Email: roode@atmos.washington.edu

Abstract

As part of the FIRE III (First ISCCP Regional Experiment) Arctic Cloud Experiment actinic flux measurements were made above the Arctic Sea ice during May 1998. FIRE III was designed to address questions concerning clouds, radiation and chemistry in the Arctic sea ice region. The actinic flux, which is also referred to as the 4π-radiative flux, is the relevant radiative parameter needed to determine photodissociation rates. Moreover, it is discussed that the actinic flux may be used to determine vertical absorption profiles of the net irradiance, provided that the single scattering albedo is known.

The diurnal cycle of UV-A (wavelength about 365 nm) and visible (wavelength about 550 nm) actinic fluxes during clear and cloudy conditions was measured by two 4π-radiometers installed just above the ice surface. In addition, vertical profiles of the visible actinic flux through low arctic stratus clouds were observed by means of a tethered balloon. The cloud thermodynamic and microphysical structure was assessed from observations made by the NCAR C-130 aircraft. The liquid water path was retrieved by a microwave radiometer.

During clear skies the diurnal variation of the actinic flux was controlled mainly by Rayleigh scattering. Above the cloud layer the actinic flux was found to be almost the same as during clear sky conditions. This could be attributed to the fact that the effective albedo of the arctic sea ice and the cloud is only slightly higher than the ground albedo alone. The observed vertical actinic flux profiles in arctic stratus are discussed and compared with similar measurements made in Atlantic stratocumulus. In the arctic stratus clouds the actinic flux was found to be nearly constant with height, except in a shallow layer near the cloud top where the actinic flux significantly increased with height. The role of the solar zenith angle and ground albedo on in-cloud actinic flux profiles is discussed. It is concluded that the observed strong increase of the actinic flux in the upper part of the arctic stratus layer is a typical feature associated with large solar zenith angles.

1. Introduction

To study the change in the concentration of a chemical reactive species in the atmosphere an elaborate set of equations describing chemical reactions has to be solved on a global scale. Many of these chemical reactions are driven by solar radiation as a result of photodissociation [*Crutzen and Zimmermann,* 1991]. The radiative parameter that determines the photodissociation rate of chemical species is the actinic flux, which is defined as the incident radiance integrated over all solid angles [*Madronich,* 1987]. The actinic flux therefore concerns the probability of an encounter between a photon and a molecule, whereas the irradiance describes the flow of radiant energy through the atmosphere [*Zeng et al.,* 1996]. Thus, radiance incident from all directions contributes to the actinic flux and for this reason it is also referred to as the mean intensity, or the 4π-radiative flux.

The computation of the actinic flux is rather complicated because it depends strongly on the ratio between the downward direct and diffuse component of the radiation, and on the amount of upward reflected radiation (*Madronich* [1987], *Ruggaber et al.* [1993], *Van Weele and Duynkerke* [1993], *Zeng et al.* [1996], *Los et al.* [1997], and *Landgraf and Crutzen* [1998]). Therefore, there is no simple linear relationship between the monochromatic actinic flux and the irradiance, as was shown from actinic flux observations reported by *Van Weele et al.* [1995]. The effect of a high surface albedo on the actinic flux was discussed on the basis of observations made by *Junkermann* [1994], *Shetter et al.* [1996], and *McKenzie et al.* [1998]. *Vilà-Guerau de Arellano et al.* [1994] presented actinic flux measurements collected by means of a tethered balloon in Atlantic stratocumulus.

Actinic fluxes were measured by the IMAU above the arctic sea ice at the SHEBA (Surface Heat Balance of the Arctic Ocean) ice camp (76˚N, 166˚W) during May, 1998. This measurement campaign was part of the FIRE III (First ISCCP (International Satellite Cloud Climatology Project) Regional Experiment) Arctic Cloud Experiment, which was designed to address questions concerning clouds and radiation in the arctic sea ice region [*Curry et al.*, 2000]. The arctic region is characterized by a high surface albedo, large solar zenith angles and the frequent occurrence of low stratus clouds. UV-A and visible actinic fluxes, at a wavelength (λ) of 365 and 550 nm, respectively, were measured continuously by two 4π-radiometers installed just above the surface, whereas vertical profiles of the visible actinic flux were obtained at least once a day from tethered-balloon observations. The visible 4π-radiometer aboard the balloon was identical to the one installed above the ice surface [*Van der Hage and De Roode*, 1999].

In section 2 some relations between the irradiance and actinic flux are summarized. In section 3 the experimental set-up is described. In section 4 the thermodynamic and microphysical structure of arctic stratus as observed from the NCAR C130 research aircraft is discussed in detail. In section 5 observations of actinic fluxes are presented. The diurnal cycle of actinic fluxes during clear sky and cloudy conditions is discussed. These results are compared with simulations performed by the Tropospheric Ultraviolet-Visible (TUV) radiation model [*Madronich*, 1993]. In addition, vertical profiles of the actinic flux measured in arctic stratus clouds are shown and compared with observations made in Atlantic stratocumulus [*Vilà-Guerau de Arellano et al.*, 1994]. In section 6 the conclusions are presented.

2. Theory

The total actinic flux (F_{tot}) can be computed by integrating the total radiance (I_{tot}) over all angles:

$$F_{tot} \equiv \int_0^{2\pi} \int_{-1}^{1} I_{tot}(\mu, \varphi) d\mu d\varphi \qquad (1)$$

where ϕ is the azimuth angle and μ is the cosine of the zenith angle θ. The total net irradiance E_{tot} is defined as:

$$E_{tot} \equiv \int_0^{2\pi} \int_{-1}^{1} I_{tot}(\mu, \varphi)\, \mu d\mu d\varphi \quad . \qquad (2)$$

In these definitions I_{tot} represents the total radiance field due to the contribution of the direct solar beam I_0 and the diffuse radiance I_*. Similarly, the actinic flux and irradiance can be decomposed into separate contributions

$$F_{tot} = F_0 + F_u + F_d = F_0 + F_* \quad , \qquad (3)$$

$$E_{tot} = -E_0 + E_u - E_d = -E_0 + E_* \qquad (4)$$

with the subscripts 'u' and 'd' representing the upward and downward components due to

diffuse radiation, the subscript '0' denotes the contribution due to the direct solar beam, the subscript '*' indicates the total net diffuse component of the actinic flux and irradiance, and μ_0 is the cosine of the solar zenith angle ($\mu_0>0$). The direct solar irradiance E_0 as a function of the optical depth is given by

$$E_0(\tau) = \mu_0 S_0(0) e^{-\tau/\mu_0} \quad , \qquad (5)$$

where S_0 is the solar irradiance perpendicular to the direction of incidence at the top of the atmosphere, $\tau = \int_z^\infty k(z')dz'$ the optical depth, and k the extinction coefficient. The direct components of the actinic flux and irradiance are related according to [*Madronich*, 1987]

$$F_0 = \frac{E_0}{\mu_0} \quad . \qquad (6)$$

An equation that describes the relation between the irradiance and the actinic flux can be derived from the radiative transfer equation for the diffuse radiance $I(\tau,\mu,\phi)$ which reads [*Goody and Yung*, 1989]

$$\mu \frac{dI(\tau, \mu, \varphi)}{d\tau} = I(\tau, \mu, \varphi) - \frac{\omega_0}{4\pi}\int P(\mu, \varphi;\mu', \varphi') I(\tau, \mu', \varphi')\, d\omega' - \frac{\omega_0}{4\pi} P(\mu, \varphi;-\mu_0, \varphi_0) S_0 e^{-\tau/\mu_0} \qquad (7)$$

with z the height above the ground surface, ω_0 the single scattering albedo, $d\omega = \sin\theta d\theta d\varphi$, $P(\mu, \varphi;\mu', \varphi')$ the phase function defining the light incident at (μ',φ') which is scattered in the direction (μ,φ). An equation describing the relation between the irradiance and the actinic flux can be derived by multiplying (7) by $d\omega$, integrate and use (6) which yields

$$\frac{dE_*}{d\tau} = (1-\omega_0)F_* - \omega_0\frac{E_0}{\mu_0} \quad , \qquad (8)$$

where we used a phase function P normalized to unity, $\int\frac{P}{4\pi}d\omega = 1$. By (4), (5) and (6) we can rewrite (8)

$$\frac{dE_{tot}}{d\tau} = (1-\omega_0)F_{tot} \quad . \qquad (9)$$

According to Eq. (9), if there is no absorption, $\omega_0 = 1$, then the total net irradiance will remain constant irrespective of changes in the optical depth, which means that radiative energy is conserved. However, for $0 < \omega_0 < 1$, and since F_{tot} is positive definite, the total net irradiance will become less negative toward cloud base, indicating that radiation is absorbed within the cloud layer. If the single scattering albedo is known very accurately, the change in the total net irradiance can then be found by measuring the total actinic flux, and integration of Eq. (9). A possible advantage of this approach is that it requires only one 4π-radiometer, rather than two separate radiometers for the downward and upward components of the irradiance. Moreover, because radiance is not weighted by a factor $\cos\theta$ in the actinic flux, the orientation of 4π-

radiometers is not of importance, whereas radiometers measuring irradiance need to be installed perfectly horizontally.

In an analogous way we can derive an equation which relates the total actinic flux to the gradient of the total net irradiance. If we multiply (7) by μdω and integrate to give

$$\int \mu^2 \frac{dI(\tau, \mu, \varphi)}{d\tau} d\omega = \int \mu I(\tau, \mu, \varphi) d\omega - \frac{\omega_0}{4\pi} \int\int \mu P(\mu, \varphi; \mu', \varphi') I(\tau, \mu', \varphi') d\omega' d\omega - \frac{\omega_0}{4\pi} \int \mu P(\mu, \varphi; -\mu_0, \varphi_0) S_0 e^{-\tau/\mu_0} d\omega \quad . \qquad (10)$$

To simplify Eq. (10) we will use the following approximation [*Goody and Yung*, 1989]

$$\int \mu^2 \frac{dI(\tau, \mu, \varphi)}{d\tau} d\omega \approx \frac{1}{3} \frac{dF_*}{d\tau} \quad , \qquad (11)$$

and the relation

$$\frac{1}{4\pi} \int \mu P(\mu, \varphi; \mu', \varphi') d\omega = g\mu' \quad , \qquad (12)$$

with g the asymmetry factor [*Goody and Yung*, 1989]. Note that (11) is exact for the Eddington approximation. By substitution of (11) and (12) into (10) we obtain the following expression

$$\frac{1}{3} \frac{dF_{tot}}{d\tau} = (1 - \omega_0 g) E_{tot} - E_0 \left(\frac{1}{3\mu_0^2} - 1 \right) \qquad (13)$$

where we used Eqs. (3-6). Eq. (13) demonstrates the nonlinear depency of the actinic flux gradient on the irradiance. If there is no absorption, and in case of fully isotropic light, E_0=0, the actinic flux decreases linearly from cloud top toward cloud base as a function of the optical depth, since E_{tot}<0. Similarly, F_{tot} always decreases from cloud top toward cloud base when $\mu_0^2 \le 1/3$, since $E_0 \ge 0$. However, if $\mu_0^2 > 1/3$, the sign of the actinic flux gradient depends on the relative magnitude of E_0 and E_{tot}.

3. Experimental set-up: Instrumentation, measurement site

The actinic flux observations were performed during May 1998 by means of a tethered balloon and were part of the FIRE arctic field program [*Curry et al.*, 2000]. In addition, continuous observations of the actinic flux were made just above the ground surface. The tethered balloon was launched from the snow-covered ice surface at the SHEBA ice camp at least once every day. The tethered-balloon measurements also included wind velocity and direction, temperature, pressure and relative humidity. The total visible actinic flux, F_{tot} according to (1), was measured by a 4π-radiometer. To prevent the instrument from being shadowed, it was hanging through a small cable about 10 m below the balloon. The measurement frequency was 0.1 Hz. The average maximum altitude typically reached by the balloon was about 1 km, which was often sufficiently high to measure well above the tops of low stratus clouds. In addition, continuous surface observations were made of the upward and downward components of the longwave, shortwave and UV-B irradiance, UV-A and visible

actinic fluxes. The cloud water content and droplet effective radius in ground fog were measured by means of a Gerber PVM-100A that was installed at about 2.2 m above the surface. In order to obtain vertical profiles in the atmospheric surface layer wind velocity and direction, temperature and humidity were measured at five different levels from a 10 m high meteorological mast [*Duynkerke and De Roode*, 2000].

The visible 4π-radiometer used for this study was newly developed for the FIRE III experiment. It has a maximum spectral response in the visible light part of the spectrum at 550 nm, and is described by *Van der Hage and De Roode* [1999]. Basically, the instrument consists of a spherical diffuser connected to a single photodiode by a light conductor. The directional response to light is largely isotropic. Two identical visible 4π-radiometers were used, one which was attached to a balloon and one which was attached to a mast at 1.5 m above the surface. Also, a newly rebuilt version of the UV-A 4π-radiometer, described by *Van der Hage et al.* [1994], was installed near the surface. Since the single scattering albedo is nearly 1 for these wavelengths, cloud radiative absorption is negligibly small. All the 4π-radiometers were calibrated against results from the monochromatic radiative transfer model TUV for clear sky conditions by comparing the measurements with the model results for a solar zenith angle of 60˚. Clear sky conditions were determined on the basis of microwave radiometer, radar and lidar data. Under these circumstances, Rayleigh scattering and surface reflection are the primary mechanisms determining the magnitude of the actinic flux. However, even under clear skies there can be scattering particles like ice crystals and aerosols. Because scattering tends to make the light diffuse, the zenith angle $\theta_0 = 60^\circ$ was chosen because at this angle the magnitude of the actinic flux does not depend on whether the light is direct or diffuse [*Madronich*, 1987]. The

input parameters that need to be specified in the model are the vertical atmospheric profile of temperature, the surface pressure and the albedo of the snow-covered sea ice. The measured broadband shortwave surface albedo at the site was approximately 0.8, which is a value typically representative for a pristine snow surface. Simultaneous measurements of the narrowband UV-B irradiance, however, indicated that the surface albedo for this waveband was slightly higher, namely about 0.9, in accordance with a model study performed by *Wiscombe and Warren* [1980] and observations presented by *Grenfell et al.* [1994]. Based on the results presented in these studies we assumed an albedo of 0.9 as being representative for the UV-A and visible light. The actinic flux measurements are estimated to be accurate within 10%.

Because FIRE, SHEBA and the ARM (Atmospheric Radiation Measurement) interacted closely various datasets that were collected near the SHEBA site are available. The NCAR C-130 aircraft took measurements near and above the SHEBA ice camp. Tethered-balloon launches were scheduled just after and before the aircraft flew over the camp. To study the cloud microphysical structure we used FSSP-100 and 260X data from the aircraft. These instruments measure cloud droplet concentrations in different bin sizes. A microwave radiometer (MWR) was operating at 23.8 and 31.4 GHz [*Liljegren*, 1994]. The 23.8 GHz channel, nearby the water vapor spectral line at 22.235 GHz, is more sensitive to water vapor than cloud liquid water and vice versa for the the 31.4 GHz channel. Measurements of the sky radiance at these two frequencies allow the simultaneous determination of the water vapor path and liquid water path (W) from a set of two linear equations. In principal, these two channels are not very sensitive to the presence of ice except for deep cloud layers with a substantial amount of large ice crystals that scatter radiation in the 23.8 and 31.4 GHz frequencies [*Adler et al.*,

1990]. The cloud optical depth can be computed by [*Stephens*, 1984]:

$$\tau = \frac{3W}{2\rho_l r_e} \qquad (14)$$

where ρ_l is the density of liquid water, and r_e the cloud droplet effective radius. The latter could be determined from the aircraft data. During SHEBA the NOAA vertically pointing Depolarization and Backscatter Unattended Lidar (DABUL) operated nearly continuously, providing information about the cloud phase [*Intrieri et al*., 2000].

4. Meteorological conditions

Between 7 and 9 May 1998 (Julian Day 127-129) a persistent low-stratus deck, capped by a strong thermal inversion, was present at the SHEBA ice camp. According to the visible light image made by the NOAA satellite (Fig. 1) there are extended white areas intersected by black lines, which are refrozen cracks in the sea ice. These cracks frequently open and cause a strong surface flux of heat and moisture, since the temperature of the open water is just slightly below 0˚C [*Pinto et al.*, 1995]. Early in the month of May, two leads opened in the vicinity of the measurement site, several hundreds meters wide. These leads froze and reopened intermittently during the month, but during the latter half of the month virtually no open water could be seen in the vicinity of the experimental site. To the northwest of the ice station, the cracks are poorly visible because of the denser arctic stratus clouds. At first glance however, it is hard to distinguish from this figure whether the white area is covered by clouds or snow only,

because the visible reflectance of a snow-covered ice surface is virtually the same as that of a cloud overlying a snow-covered ice surface. On the right of the visible image there is a whiter spot which is indicated in the figure as a 'clear' area; the same area looks black in the infrared image. In the infrared image the whiter areas represent high clouds which have a much larger thermal contrast with the snow-covered sea ice than the low stratus clouds.

An example of the vertical potential temperature structure in arctic stratus is presented in Fig. 2. The nearly constant potential temperature in the boundary layer is a feature which is remarkably different from a vertical profile made in subtropical stratus or stratocumulus clouds. Because the wet-adiabatic lapse rate approaches the dry-adiatic lapse rate for temperatures well below freezing temperature, it is hard to distinguish a pronounced wet-adiabatic vertical temperature profile in this arctic cloud layer. The time variations of the potential temperature in the boundary layer and free atmosphere were very small; on average an upward and downward balloon sounding took about 1 hour and during this period the difference in potential temperature at the same height was less than 0.5˚C.

The NCAR C-130 aircraft flew above the SHEBA ice camp just after the balloon sounding. Cloud droplet size distributions were measured by an FSSP-100 (with a diameter (d) range $1.9<d<55.5$ μm) and by a 260X probe. Data from the latter were used for particles with a diameter $60.4<d<846.4$ μm; thus measurements from the smallest bins were neglected to prevent overlaps with the FSSP bins. Neither instrument can distinguish whether the collected particles are in the ice or liquid water phase. To compute the liquid and ice water content and the cloud droplet effective radius it was assumed that the droplets were spherical. This assumption

is not very accurate for large particles which are detected by the 260X. These are probably ice or snow particles, but as can be seen in Fig. 3a, their contribution to the ice and liquid water content (IWC and LWC, respectively) is relatively low, as is their number concentration. The results of the IWC and LWC shown in the figure are the averages of all data collected within height intervals of 10 m. The cloud droplet effective radius and the droplet number concentration are mean values computed for IWC+LWC>0.001 gm^{-3}, in order to filter effects caused by instrumental noise. If we define this threshold to distinguish between clear and cloudy air, we find that between 290 and 380 m the cloud fraction was about unity. The total IWC and LWC in the cloud layer is due primarily to the smaller droplets which were measured by the FSSP. As a result, r_e above cloud base (~300 m during the aircraft measurements) is relatively small and of the order of 5 μm. This relatively small number is due to a rather high cloud ice and liquid water droplet concentration of about 250 cm^{-3}.

Herman and Curry [1984] presented droplet spectra of arctic stratus clouds and concluded that the clouds had a wide range of microphysical properties, and their measured values of the total cloud droplet concentration were as large as 512 cm^{-3}. In the subcloud layer the larger particles measured by the 260X dominate, as is clear by the contribution they make to the IWC and LWC. As a consequence, r_e is about one order of magnitude larger than in the cloud layer. These results are similar to observations made in marine stratocumulus [*Duynkerke et al*., 1995]. They concluded that within the cloud layer the liquid water content was due mainly to the smaller droplets, whereas in the subcloud layer larger droplets dominated making a negligibly small contribution to the liquid water content but, on the other hand, causing a significant amount of drizzle.

Fig. 4 shows the cloud optical depth computed by Eq. (16), where we used r_e= 5 μm according to the aircraft measurements and MWR data were used for the liquid water path. The cloud layer tended to become optically thinner around the time of maximum solar elevation, which occurred around 23:00 UTC. Usually arctic stratus clouds are predominantly optically thin [*Curry et al*., 1996]. Because the cloud droplet effective radius was relatively low, rather high maximum values of the optical depth were found ($\tau_{max} \approx 20$). These maxima were typically observed during low μ_0. Since the MWR is insensitive to the presence of ice these results indicate that a significant fraction of the cloud particles consisted of liquid water droplets, in spite of the relatively cold temperatures in the cloud (about -18˚C). The lidar depolarization ratio δ can serve as an indicator of cloud phase. Nearly spherically symmetrical and optically homogeneous scatterers, such as cloud and drizzle drops, generate near-zero depolarization of the incident energy in the exact backscattering direction, while scatterers with the arbitrary geometry of ice particles, on the other hand, generate values which are typically in the range $\delta \approx 0.4 - 0.5$ [*Sassen*, 1991]. The lidar depolarization ratio was small for this period (δ<0.1), suggesting that the cloud phase was predominantly liquid. Analyses of other NCAR C-130 data measured during SHEBA suggested that in the absence of ice particles falling from above the occurence of ice in boundary layer clouds appears to be related to maximum droplet sizes [*Curry et al*., 2000]. Based on these observations, and previous measurements reported by *Hobbs and Rangno* [1998], they suggested that the chance that clouds do not contain ice particles increases for larger droplet concentrations (typically >100 cm^{-3}).

A summary of the tethered-balloon soundings made between 7 and 9 May 1998 is presented in Table 1. The table also includes some characteristics of an Atlantic stratocumulus

case. The actinic flux measurements made in this cloud, and discussed in detail by *Vilà-Guerau de Arellano et al.* [1994], will be used to compare with the observations made in arctic stratus.

5. Results

5.1. Diurnal cycle

In Fig. 5 observed actinic fluxes for a clear sky day ($\tau = 0$) are presented and compared with model results. The observed actinic fluxes are slightly smaller than the model results. By $\tau = 0$, we implicitly assumed that aerosols and ice crystals may be neglected as scattering particles. However, it is likely that the neglect of these particles can explain the small overestimation of the modeled actinic flux. For example, if a very small optical depth was used in the model, $\tau = 0.1$, a better agreement between observed and modeled UV-A and visible actinic fluxes was found. In the figure we also plotted the theoretical value of the actinic flux for the special case of zero optical depth ($\tau = 0$), and zero ground surface albedo. For that case, by Eqs. (5) and (6), we would expect the actinic flux to be constant with time and independent of the solar zenith angle. The observations show that even for small μ_0 the actinic flux above the arctic sea ice is larger than the direct component of the actinic flux at the top of the atmosphere. As an explanation, the high surface albedo (α) acts to strongly increase the upward component of the radiation, which, by Eq. (1), enhances the total actinic flux. *Van Weele et al.* [1995] presented UV-A actinic flux measurements made during clear sky conditions for both a snow-covered ($\alpha = 0.9$) and a grass surface ($\alpha = 0.05$). They concluded that the effect of the snow was to nearly double the actinic flux in comparison with the actinic flux results found above the

grass surface.

In Fig. 6a the observed actinic flux above stratus clouds, and surface observations during both clear and cloudy skies are presented. The surface observations during cloudy skies and one of the balloon soundings (case 5) were made simultaneously. The actinic flux above the cloud is nearly the same as during the clear sky observations. This can be explained by the fact that the effective albedo of the arctic sea ice and the cloud is only slightly larger than the ground albedo alone. Below the cloud, however, the actinic flux is lower than during clear sky conditions. To examine the effect of cloud optical thickness on the actinic flux we performed a series of simulations with the TUV radiation model where we varied the solar zenith angle and optical thickness (Fig. 6b). We assumed a perfectly clear sky above the cloud (τ=0). The actinic flux above the cloud does hardly depend on the optical thickness of the cloud. Below the cloud there is a clear tendency towards a lower actinic flux with increasing optical thickness. The observations and the model results show a qualitatively similar behaviour. This should be the case since throughout the observational period the optical thickness varied between 5 and 20. The model predicts a slightly higher actinic flux above the cloud than do the observations, which probably can be explained by the fact that we neglected the effect of aerosols and ice crystals above the cloud layer.

5.2. Vertical profiles

To illustrate the effect of the solar zenith angles on the vertical profiles of the

actinic fluxes, two examples of vertical actinic flux profiles are shown in Fig. 7. These were made above the arctic sea ice and from the Santa Maria Island during the Atlantic Stratocumulus Transition Experiment (ASTEX). The ground albedo for UV-A during ASTEX was about 0.05. Although the two profiles were measured at a different wavelength (F_{365} and F_{550} for the Azores and Arctic, respectively), the fraction of diffuse light due to Rayleigh scattering is about the same for both cases. According to a computation of the optical depth for Rayleigh scattering [*Slingo and Schrecker*, 1982], the fraction τ_{Ray}/μ_0 gives 0.62 and 0.73 for the UV-A and visible radiation for the upward sounding, respectively. The measurements show that the UV-A actinic flux increases approximately linearly towards the cloud top. In contrast, the visible actinic flux has its largest divergence in the upper 50 m near the cloud top, below which the vertical variations are relatively small. Variations in μ_0 do change the magnitude of the actinic flux, but hardly affect the gross shape of the vertical profile.

The differences in the vertical profiles can be explained by means of a delta-Eddington model [*Meador and Weaver*, 1980]. Although more accurate models are available, in particular for small μ_0, this simple model can help to qualitatively understand the observed vertical profiles of the actinic flux. Four vertical profiles were computed, two of which were representative for the measurements shown in Fig. 7, and two additional simulations were made where we changed the ground albedo.

The effect of a larger ground albedo is to increase the actinic flux magnitude rather than to change the approximate shape of the vertical profile, which is more affected by the solar zenith angle (see Fig. 8). For the two cases where μ_0= 0.8, the actinic flux increases from

cloud base to a maximum just below the cloud top. This peak can be explained by Eq. (13). The irradiance and actinic flux profiles as computed by the delta-Eddington model are exacly described by this formula. Between the level of the actinic flux maximum and cloud top we have $(d/d\tau)F_{tot} > 0$, such that

$$E_0\left(\frac{1}{3\mu_0^{\,2}} - 1\right) > (1 - \omega_0 g)E_{tot} \quad . \qquad (15)$$

At the level of the actinic flux maximum these two terms balance. However, when the direct solar beam propagates into the cloud layer E_0 gradually decreases according to Eq. (5). Below the actinic flux maximum (15) does not hold anymore and the actinic flux decreases toward cloud base. For the arctic stratus cases the direct component of the solar beam E_0 enhances the downward decrease of the actinic flux in a shallow layer near the top of the cloud. Since μ_0 is so small for these cases E_0 rapidly becomes negligibly small, and the vertical gradient of the actinic flux in the bulk of the cloud layer is primarily determined by the first term on the rhs of Eq. (5)

$$\frac{dF_{tot}}{d\tau} \approx 3(1 - \omega_0 g)E_{tot} \quad . \qquad (16)$$

The very small vertical gradient of the actinic flux in the lower part of the arctic cloud layer is due to the rather low value of the total net irradiance associated with low values of μ_0.

Although the model results indicate a peak in the actinic flux for large μ_0 there is no clear peak value to be distinguished from the balloon sounding made from the Azores. This could be due to the fact that in a real cloud field the cloud tops are located at different heights such that the peak value is smoothed, whereas in the model a perfectly homogeneous cloud is assumed. Nevertheless, the basic features of the observed vertical profiles, such as the strong increase below the cloud top for low μ_0, can be explained qualitatively well by the delta-Eddington model.

6. Conclusion and discussion

The actinic flux is the radiative quantity that determines photodissociation rates in the atmosphere. Actinic flux measurements were made above the arctic sea ice by means of a tethered balloon and from surface observations. The arctic sea ice region is characterized by a high surface albedo, large solar zenith angles and the frequent occurrence of low stratus clouds. We have discussed the diurnal cycle of the actinic flux near the surface for clear and cloudy conditions. In addition, we have presented vertical profiles of the actinic flux in and above arctic stratus. To analyse the thermodynamic and microphysical structure of a persistent arctic stratus cloud in detail we have used NCAR C-130 aircraft data that were collected above the measurement site.

Between 7 and 9 May 1998 a persistent arctic stratus layer was present above the SHEBA ice camp. The temperature of the cloud layer was low (about -18˚C) and the cloud top

was capped by a stable temperature inversion. The cloud droplet concentration was rather high (about 250 cm^{-3}). The liquid water path of the cloud, as retrieved by a microwave radiometer, was suggesting that a significant amount of the cloud droplets were supercooled. This finding was corroborated by the rather low depolarization ratios obtained by a lidar during this period, which are indicative of spherical liquid water droplets. This type of arctic stratus cloud layer was frequently observed during other aircraft flights performed during the SHEBA project. *Curry et al.* [2000] suggested that the presence of ice particles in arctic clouds would be more likely if the cloud droplet concentration is rather low. Conversely, the cloud phase would tend to be liquid if there is a higher cloud droplet concentration (>100 cm^{-3}).

From the actinic flux observations near the surface it was shown that for clear sky conditions the magnitude of the actinic flux is primarily determined by Rayleigh scattering and ground reflection. Above the cloud the magnitude of the actinic flux was found to be nearly the same as during clear sky conditions, mainly because the optical properties of the snow-covered ice surface resemble those of a cloud surface above a snow-covered ice surface.

The vertical actinic flux gradient was found to be very small within the arctic stratus cloud, except in a shallow layer near the cloup top where the actinic flux significantly increased with height. This observed shape was explained by a manipulation of the radiative transfer equation for the diffuse radiance. It was discussed that if the direct component of the radiation is negligibly small and there is no absorption in the cloud, the actinic flux will linearly decrease from cloud top to the cloud base as a function of the optical depth. The slope of the vertical gradient is proportional to the magnitude of the net irradiance. Because the arctic stratus

observations were made during rather small values of μ_0, the vertical actinic flux gradient was very small too. In contrast, for large μ_0, and much larger values of the net irradiance, the actinic flux will significantly decrease from the cloud top towards the cloud base, as was found by *Vilà-Guerau de Arellano et al.* [1994] in Atlantic stratocumulus. Deviations from this linear vertical actinic flux profile can be expected if the direct contribution of the direct solar radiation may not be neglected. This is usually the case near the cloud top, where it can cause a significant increase with height if $\mu_0^2<1/3$, as was observed in the arctic stratus clouds.

It has been demonstrated that a tethered balloon is a good platform to measure actinic fluxes. Since the actinic flux is intimately related to the irradiance, it is a valuable parameter to measure during intensive field campaigns. For the observations discussed in this paper, radiative absorption was negligible small. We have explained, however, that there is a simple relation between the magnitude of the actinic flux and the gradient of the irradiance. For wavelengths which have a single scattering albedo less then unity, actinic flux observations may therefore be used to measure absorption profiles of the total net irradiance indirectly.

Acknowledgements

Michiel van Weele is thanked for his assistance with the radiative transfer model. The first author was supported by the Netherlands Geosciences Foundation (GOA) with financial aid (Grant 750.295.03A) from the Netherlands Organization for Scientific Research. The aircraft data collected by means of the C-130 of NCAR were kindly supplied by Ron Ruth

and Krista Laursen. The authors thank NCAR and its sponsor, the National Science Foundation, for allowing them to use the observational data. The microwave radiometer data were kindly provided by Dr. J. Liljegren (Iowa State University). The satellite figures presented in this paper were made by Dr. D. Wylie (University of Wisconsin). Finally, the authors wish to thank the many people of the FIRE/SHEBA community for giving logistical support by bringing the equipment to the SHEBA ice camp and for assisting on the site.

References

Adler, R. F., R. A. Mack, N. Prasad, I. M. Hakkarinen, H.-Y. M. Yeh, Aircraft microwave observations and simulations of deep convection from 18 to 183 GHz. Part I: Observations. *J. Atmos. Oceanic Technol., 7*, 377-391, 1990.

Crutzen, P. J., and P. H. Zimmermann, The changing photochemistry of the atmosphere, *Tellus, 43AB*, 136-151, 1991.

Curry, J. A., and 26 Coauthors, FIRE arctic clouds experiment, *Bull. Amer. Meteor. Soc., 81*, 5-30, 2000.

Duynkerke, P. G., H. Q. Zhang, and P. J. Jonker, Microphysical and turbulent structure of nocturnal stratocumulus as observed during ASTEX, *J. Atmos. Sci., 52, 2763-2777*, 1995.

Duynkerke, P. G, and S. R. De Roode, Surface energy balance and turbulence characteristics observed at the SHEBA ice camp during FIRE III. *J. Geophys. Res., submitted for the special FIRE III issue*, 2000.

Goody, R. M., and Y. L. Yung, *Atmospheric radiation. Theoretical basis*, 2nd Ed., 519 pp., Oxford University Press, 1989.

Grenfell, T. C., S. G. Warren, and P. C. Mullen, Reflection of solar radiation by the Antarctic snow surface at ultraviolet, visible, and near-infrared wavelengths, *J. Geophys. Res., 99*, 18,669-

18,684, 1994.

Herman, G. F., and J. A. Curry, Observational and theoretical studies of solar radiation in Arctic stratus clouds, *J. Climate Appl. Meteor., 2*3, 5-24, 1984.

Hobbs, P. V., and A. L. Rangno, Microstructures of low- and middle-level clouds over the Beaufort Sea. *Quart. J. Roy. Meteor. Soc., 124,* 2035-2071, 1998.

Intrieri, J. M., M. D. Shupe, B. J. McCarty, and T. Uttal, 2000: Annual cycle of arctic cloud statistics from lidar and radar at SHEBA. *J. Geophys. Res., submitted.*

Junkermann, W., Measurements of the J(O1D) actinic flux within and above stratiform clouds and above snow surfaces, *Geophys. Res. Lett., 21*, 793-796, 1994.

Landgraf, J., and P. J. Crutzen, An efficient method for online calculations of photolysis and heating rates, *J. Atmos. Sci., 55, 863-878*, 1998.

Liljegren, J. C., Two-channel microwave radiometer for observations of total column precipitable water vapor and cloud liquid water path. Proc. Fifth Symp. on Global Change Studies, Nashville, TN, Amer. Meteor. Soc., 262-269, 1994.

Los, A., M. van Weele, and P. G. Duynkerke, Actinic fluxes in broken cloud fields, *J. Geophys. Res., 102*, 4257-4266, 1997.

Madronich, S., Photodissociation rates in the atmosphere. 1. Actinic flux and the effects of ground reflections and clouds, *J. Geophys. Res., 92*, 9740-9752, 1987.

Madronich, S., *UV radiation in the natural and perturbed atmosphere, in Environmental effects of UV (Ultraviolet) Radiation*, pp. 17-69, CRC Press, Boca Raton, 1993.

McKenzie, R. L., K. J. Paulin, and S. Madronich, Effects of snow cover on UV irradiance and surface albedo: A case study, *J. Geophys. Res., 103*, 28,785-28,792, 1998.

Meador, W. E., and W. R. Weaver, Two-stream approximations to radiative transfer in planetary atmospheres: A unified description of existing methods and a new improvement, *J. Atmos. Sci., 37*, 630-643, 1980.

Pinto, J. O., J. A. Curry, and K. L. McInnes, Atmospheric convective plumes emanating from leads. 1: Thermodynamic structure, *J. Geophys. Res., 100*, 4621-4631, 1995.

Ruggaber, A., R. Forkel, and R. Dlugi, Spectral actinic flux and its ratio to irradiance by radiation transfer calculations, *J. Geophys. Res., 98*, 1151-1162, 1993.

Sassen, K., The polarization lidar technique for cloud research: A review and current assessment. *Bull. Amer. Meteor. Soc., 72*, 1848-1866, 1991.

Shetter, R. E., C. A. Cantrell, K. O. Lantz, S. J. Flocke, J. J. Orlando, G. S. Tyndall, T. M. Gilpin, C. A. Fischer, S. Madronich, and J. G. Calvert, Actinometric and radiometric measurement and modeling of the photolysis rate coefficient of ozone to O(1D) during Mauna Loa observatory photochemistry experiment 2, J. *Geophys. Res., 101*, 14,631-14,641, 1996.

Slingo, A., and H. M. Schrecker, On the short-wave radiative properties of stratiform water clouds, *Quart. Roy. Meteor. Soc., 108*, 407-426, 1982.

Stephens, G. L., The parameterization of radiation for numerical weather prediction and climate models, *Mon. Wea. Rev., 112*, 826-867, 1984.

Van der Hage, J. C. H., W. Boot, H. van Dop, P. G. Duynkerke, and J. Vilà-Guerau de Arellano, A photo-electric detector suspended under a balloon for actinic-flux measurements, *J. Atmos. Oceanic. Technol.*, 11, 674-679, 1994.

Van der Hage, J. C. H., and S. R. de Roode, An isotropic light sensor for measurements of visible actinic flux in clouds, *J. Atmos. Oceanic. Technol., 16*, 1698-1701, 1999.

Van Weele, M., P. G. Duynkerke, Effect of clouds on the photodissociation of NO2: observations and modelling, *J. Atmos. Chem., 16*, 231-255, 1993.

Van Weele, M, J. Vilà-Guerau de Arellano, and F. Kuik, Combined measurements of UV-A actinic flux, UV-A irradiance and global radiation in relation to photodissociation rates, *Tellus*,

47B, 353-364, 1995.

Vilà-Guerau de Arellano, J., P. G. Duynkerke and M. van Weele, Tethered-balloon measurements of actinic flux in a cloud-capped marine boundary layer, *J. Geophys. Res. , 99*, 3699-3705, 1994.

Wiscombe, W. J., and S. G. Warren, A model for the spectral albedo of snow. 1: Pure snow, *J. Atmos. Sci., 37*, 2712-2733, 1980.

Zeng, J., S. Madronich, and K. Stamnes, A note on the use of the two-stream delta-scaling approximation for calculating atmospheric photolysis rate coefficients, *J. Geophys. Res. , 101*, 14,525-14,530, 1996.

Tables

Table 1: Cloud characteristics for the five selected tethered-balloon soundings made above the Arctic Sea ice, and case 5 from *Vilà-Guerau de Arellano et al.* [1994] measured during the ASTEX experiment on Santa Maria Island on 13 June 1992, Azores (36.99˚N, 25.17˚W). The values of μ_0 represent values of the cosine of the solar zenith angle at the start of the upward sounding and the end of the downward sounding. The cloud cover for the Arctic stratus cases was approximately unity, whereas the Atlantic stratocumulus case was mostly broken to overcast (N=7 oktas and N=8 oktas).

case	start Julian day (decimal)	μ_0 start	μ_0 end	$\bar{\tau}$	cloud type
2	127.73	0.30	0.36	5 ± 2	stratus
5	128.77	0.36	0.42	17 ± 4	stratus
7	129.17	0.33	0.27	12 ± 4	stratus
8	129.31	0.15	0.10	10 ± 4	stratus, thinning throughout experiment
9	129.80	0.40	0.45	8 ± 4	fog
Azores	165.66	0.85	0.74	23 ± 4	stratocumulus

Figure captions

Figure 1. NOAA AVHRR satellite images at 22:19 UTC, 7 May 1998 over the SHEBA ice camp remapped to a polar stereographic project (1 km). (a) Channel 1 (0.63 micron) visible satellite image. Black lines are old cracks in the ice that have refrozen. Whiter parts of the image are clearer areas than the darker (cloudier) parts. Ice patterns are poorly visible to the northwest of the ice station because of the denser arctic stratus cloud. (b) Infrared channel 4 (11 micron). Darker parts of the image are clearer areas than the lighter (cloudier) parts. Ice patterns cannot be seen through the optically denser (whiter) clouds.

Figure 2. Vertical potential temperature profile measured from the tethered balloon on 7 May 1998 around 18:00 UTC. Indicated are the approximate cloud base (260 m) and cloud top (450 m) during the balloon sounding.

Figure 3. NCAR C-130 aircraft FSSP-100 and 260X data collected between 21:06 and 0:51 UTC just after a balloon sounding on 7 May 1998 (Figure 2). (a) Ice (IWC) and liquid water content (LWC). (b) Droplet concentration. (c) Cloud droplet effective radius. The balloon and aircraft measurements were made with a frequency of 0.1 Hz and 1 Hz, respectively. The aircraft speed was about 100 m/s.

Figure 4. The cloud optical depth τ as a function of time. The optical depth is computed from Eq. (14) where we used the liquid water path from the microwave radiometer and the effective radius according to the aircraft data. The times of the balloon soundings are indicated by arrows,

and numbered for easy referencing.

Figure 5. Diurnal cycle of modeled (solid lines) and measured (dashed lines) actinic flux during clear skies as a function of $\mu_0 = \cos \theta_0$. (a) UV-A. (b) Visible.

Figure 6. (a) Visible actinic flux from measurements made just above the surface and from four tethered-balloon soundings in Arctic stratus. During the surface measurements arctic stratus was present from Julian day 128.46 to 128.96. The balloon soundings are summarized in Table 1. (b) Model simulation of the visible actinic flux below, and above the cloud for different values of the optical thickness (τ).

Figure 7. Measured vertical profiles of the actinic flux. (a) UV-A actinic flux in stratocumulus during ASTEX. (b) Visible actinic flux in Arctic stratus above Arctic sea ice (case 8 according to Table 1). Also indicated are the cloud base and cloud top height. During the ASTEX stratocumulus sounding the cloud-base height descended when the balloon was descending, and the indicated cloud top and cloud base height are taken for the upward sounding.

Figure 8. Vertical profiles of the actinic flux in the cloud layer, normalized with the incident actinic flux at the top of the atmosphere, calculated with the delta-Eddington model.

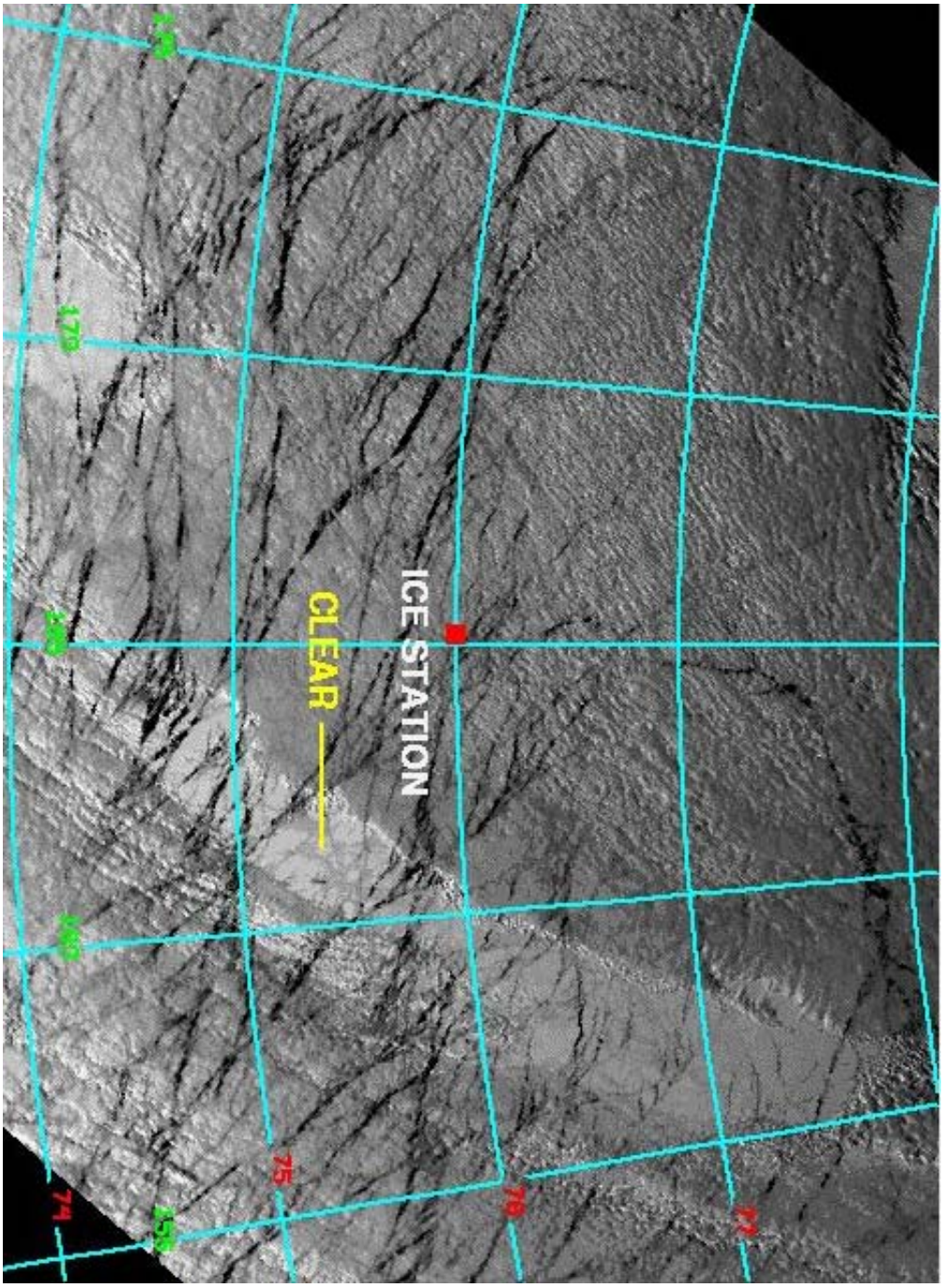

Figure 1(a). NOAA AVHRR satellite images at 22:19 UTC, 7 May 1998 over the SHEBA ice camp remapped to a polar stereographic project (1 km). Channel 1 (0.63 micron) visible satellite image. Black lines are old cracks in the ice that have refrozen. Whiter parts of the image are clearer areas than the darker (cloudier) parts. Ice patterns are poorly visible to the northwest of the ice station because of the denser arctic stratus cloud.

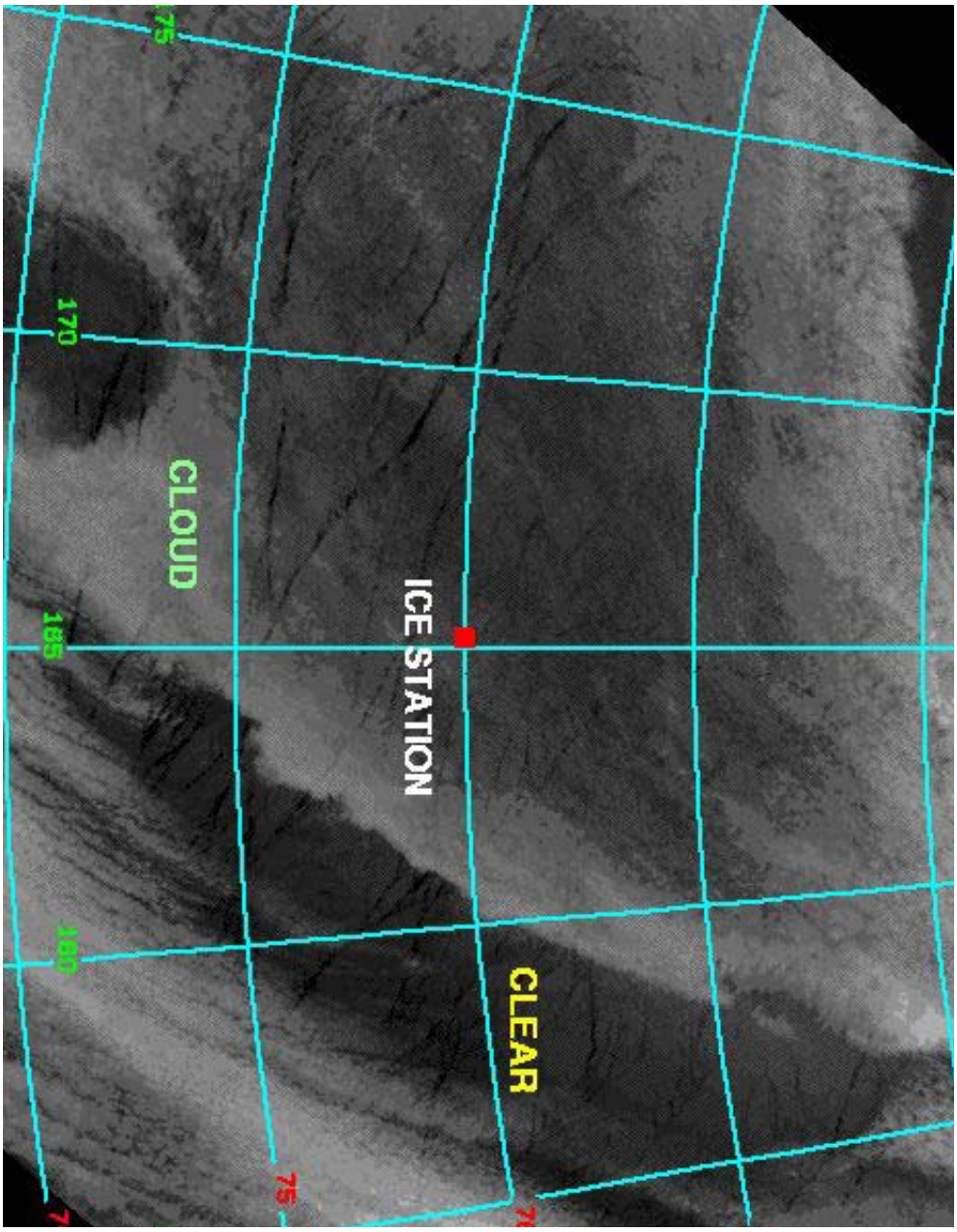

Figure 1(b). NOAA AVHRR satellite images at 22:19 UTC, 7 May 1998 over the SHEBA ice camp remapped to a polar stereographic project (1 km). Infrared channel 4 (11 micron). Darker parts of the image are clearer areas than the lighter (cloudier) parts. Ice patterns cannot be seen through the optically denser (whiter) clouds.

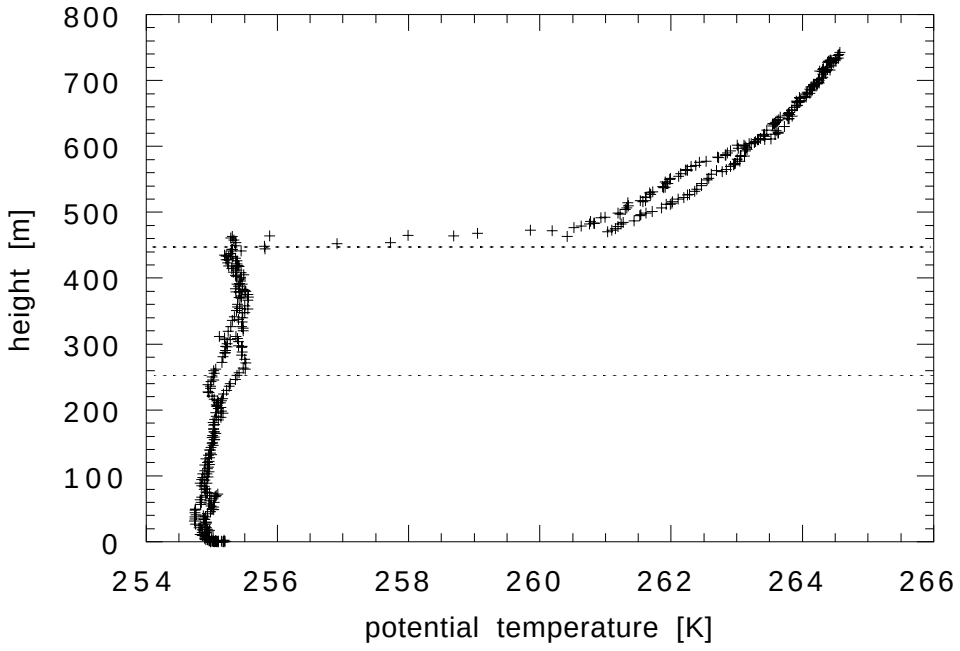

Figure 2. Vertical potential temperature profile measured from the tethered balloon on 7 May 1998 around 18:00 UTC. Indicated are the approximate cloud base (260 m) and cloud top (450 m) during the balloon sounding.

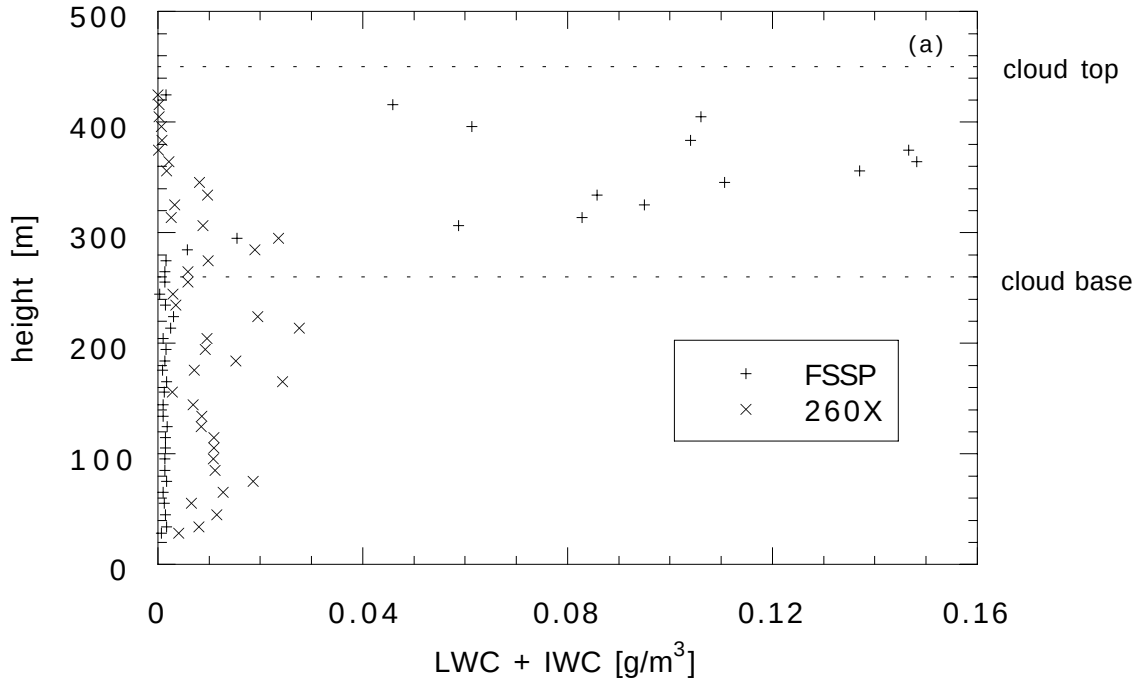
(a)
cloud top
cloud base
FSSP
260X
height [m]
LWC + IWC [g/m3]
0
100
200
300
400
500
0
0.04
0.08
0.12
0.16

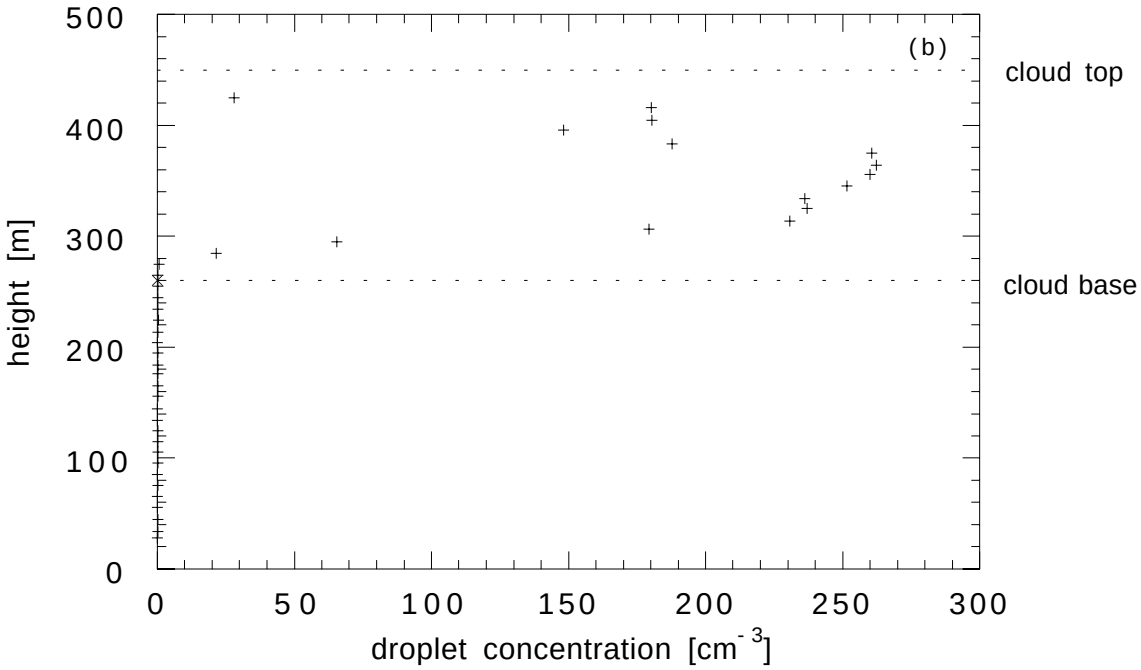
(b)
cloud top
cloud base
height [m]
droplet concentration [cm-3]
0
100
200
300
400
500
0
50
100
150
200
250
300

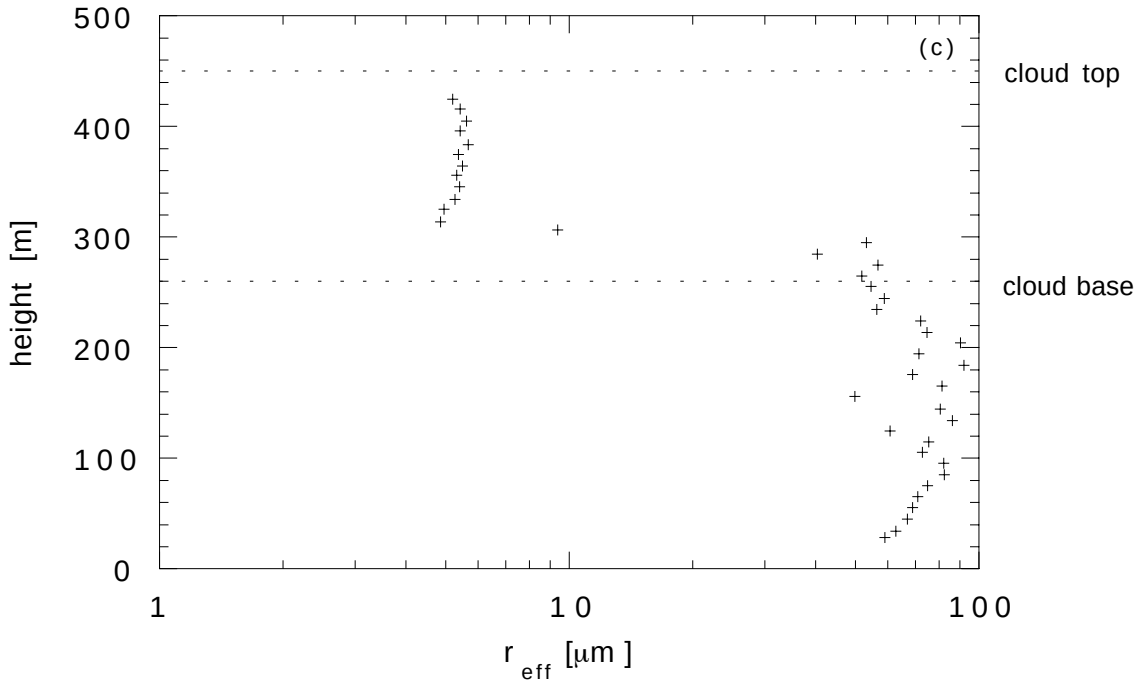

Figure 3. NCAR C-130 aircraft FSSP-100 and 260X data collected between 21:06 and 0:51 UTC just after a balloon sounding on 7 May 1998 (Figure 2). (a) Ice (IWC) and liquid water content (LWC). (b) Droplet concentration. (c) Cloud droplet effective radius. The balloon and aircraft measurements were made with a frequency of 0.1 Hz and 1 Hz, respectively. The aircraft speed was about 100 m/s.

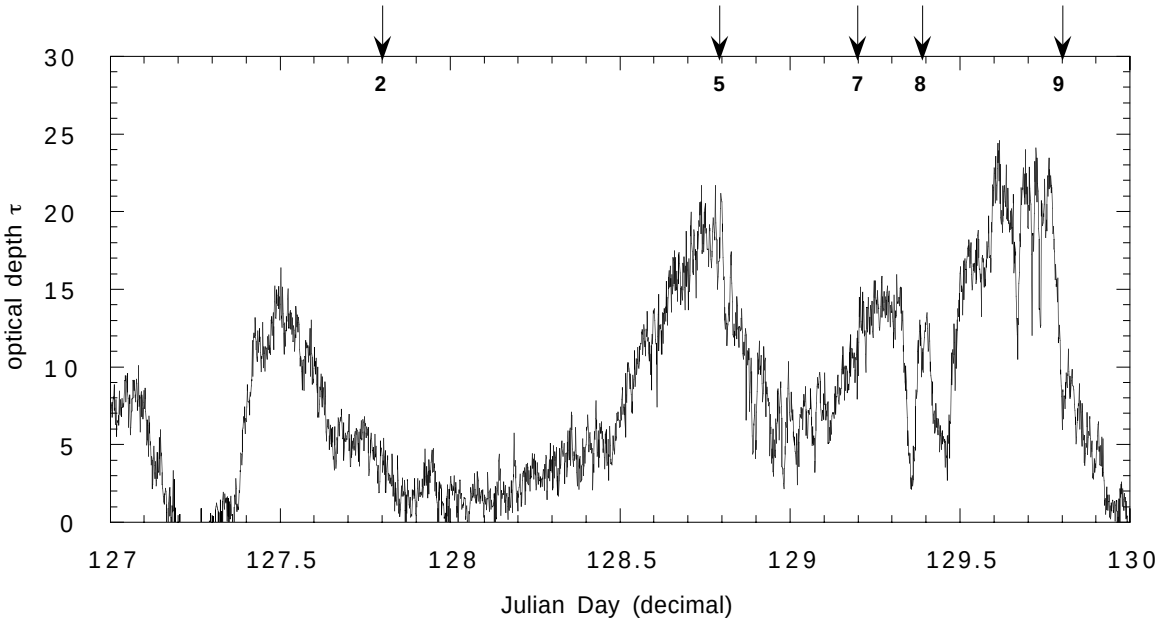

Figure 4. The cloud optical depth τ as a function of time. The optical depth is computed from Eq. (14) where we used the liquid water path from the microwave radiometer and the effective radius according to the aircraft data. The times of the balloon soundings are indicated by arrows, and numbered for easy referencing.

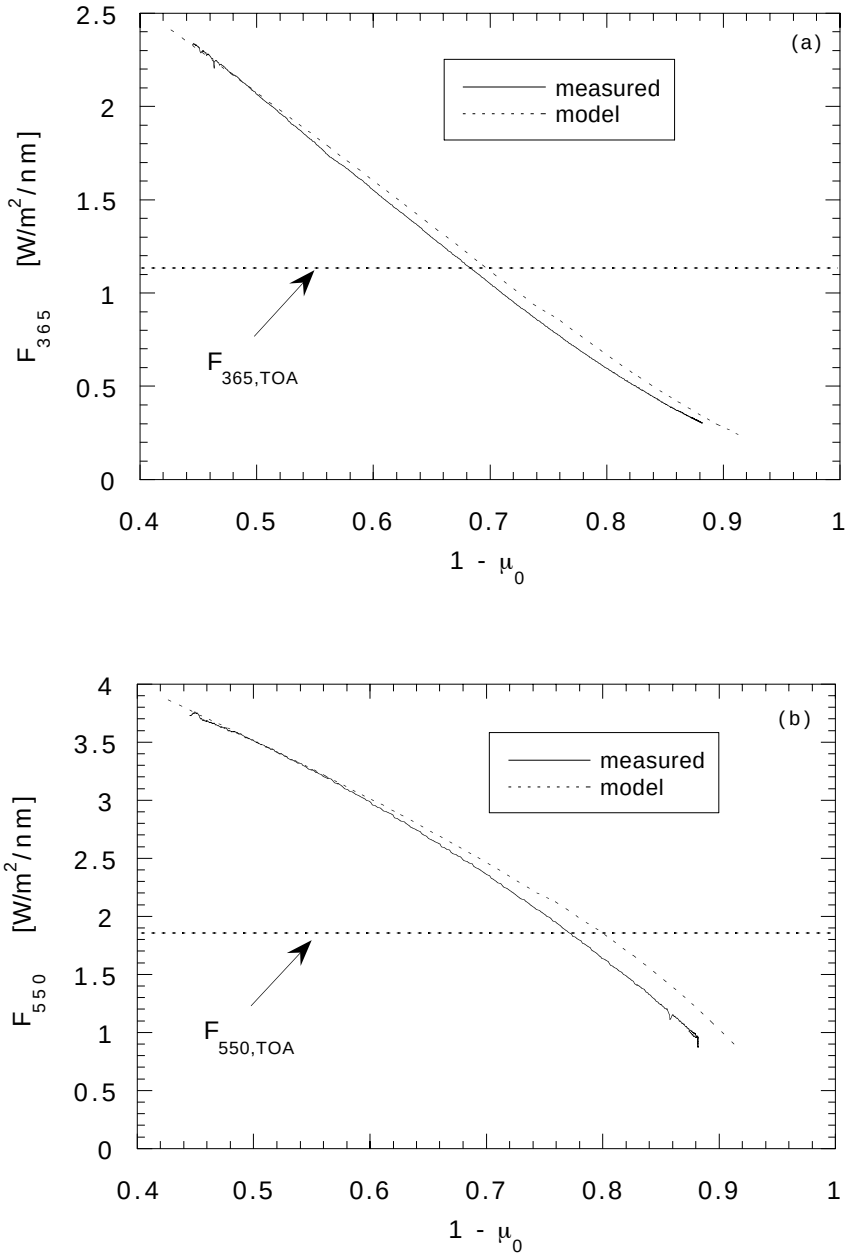

Figure 5. Diurnal cycle of modeled (solid lines) and measured (dashed lines) actinic flux during clear skies as a function of $\mu_0 = \cos \theta_0$. (a) UV-A. (b) Visible.

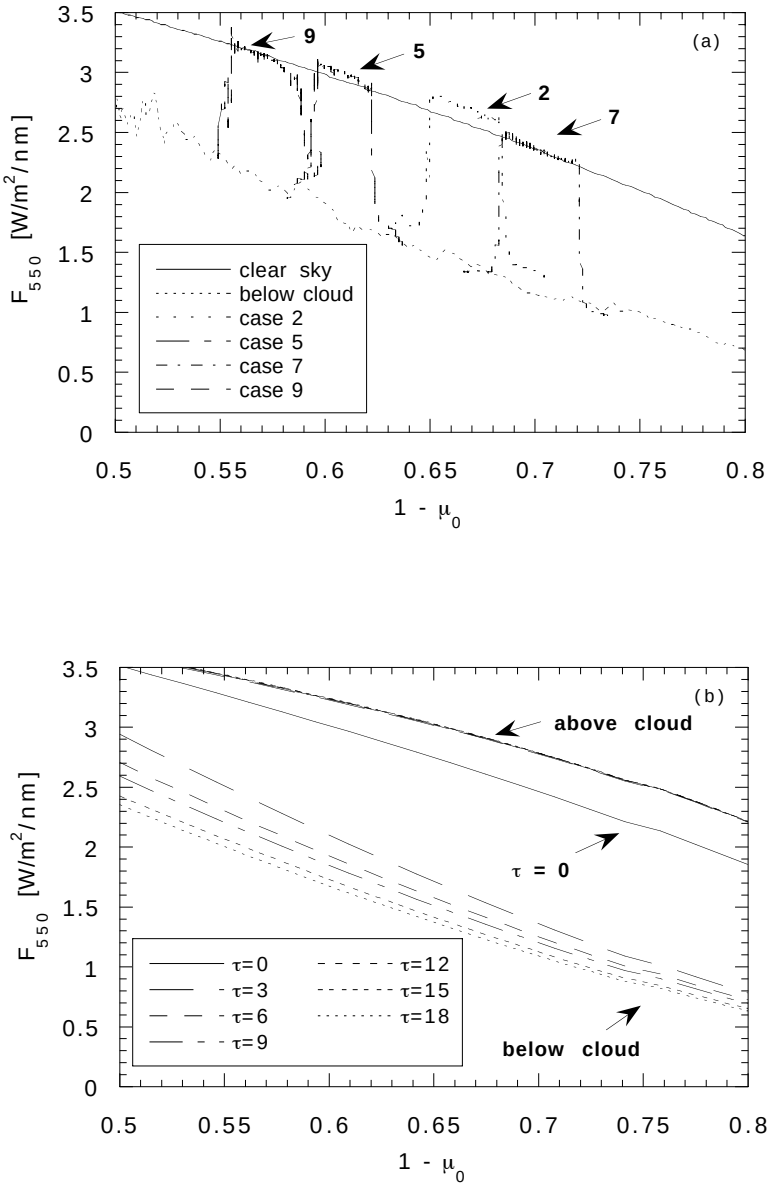

Figure 6. (a) Visible actinic flux from measurements made just above the surface and from four tethered-balloon soundings in Arctic stratus. During the surface measurements arctic stratus was present from Julian day 128.46 to 128.96. The balloon soundings are summarized in Table 1. (b) Model simulation of the visible actinic flux below, and above the cloud for different values of the optical thickness (τ).

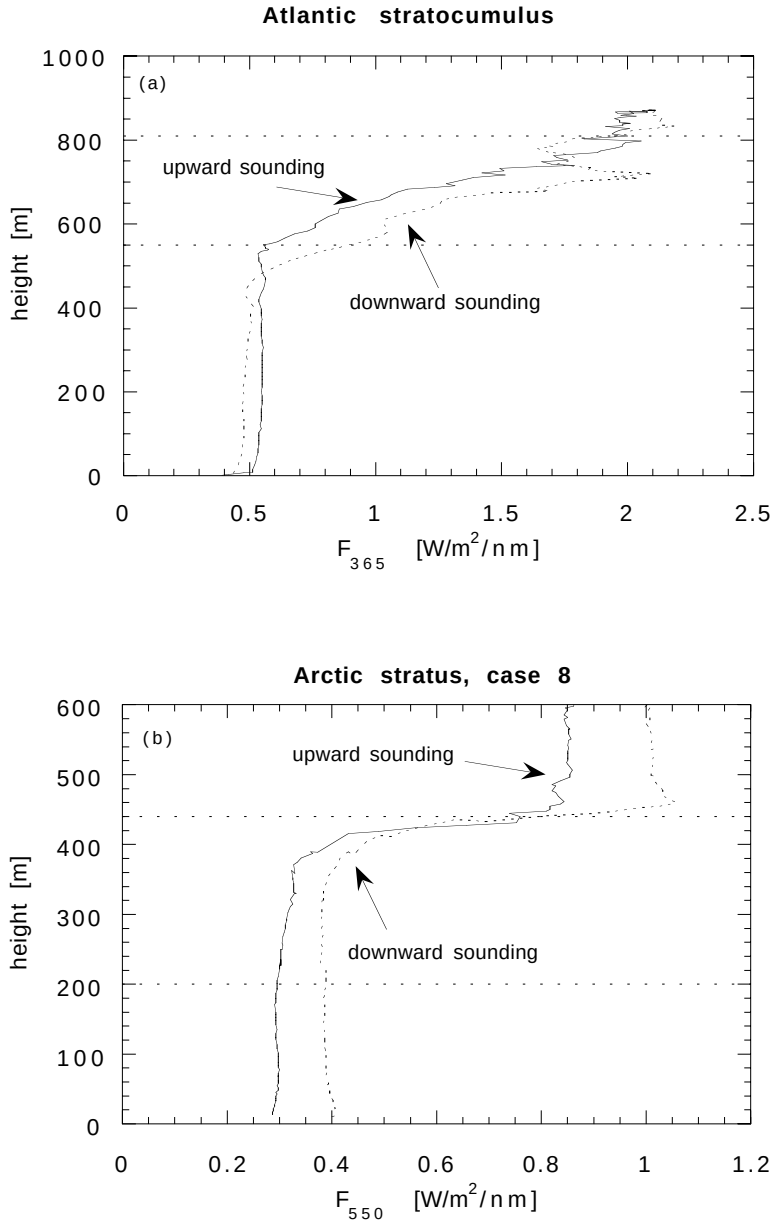

Figure 7. Measured vertical profiles of the actinic flux. (a) UV-A actinic flux in stratocumulus during ASTEX. (b) Visible actinic flux in Arctic stratus above Arctic sea ice (case 8 according to Table 1). Also indicated are the cloud base and cloud top height. During the ASTEX stratocumulus sounding the cloud-base height descended when the balloon was descending, and the indicated cloud top and cloud base height are taken for the upward sounding.

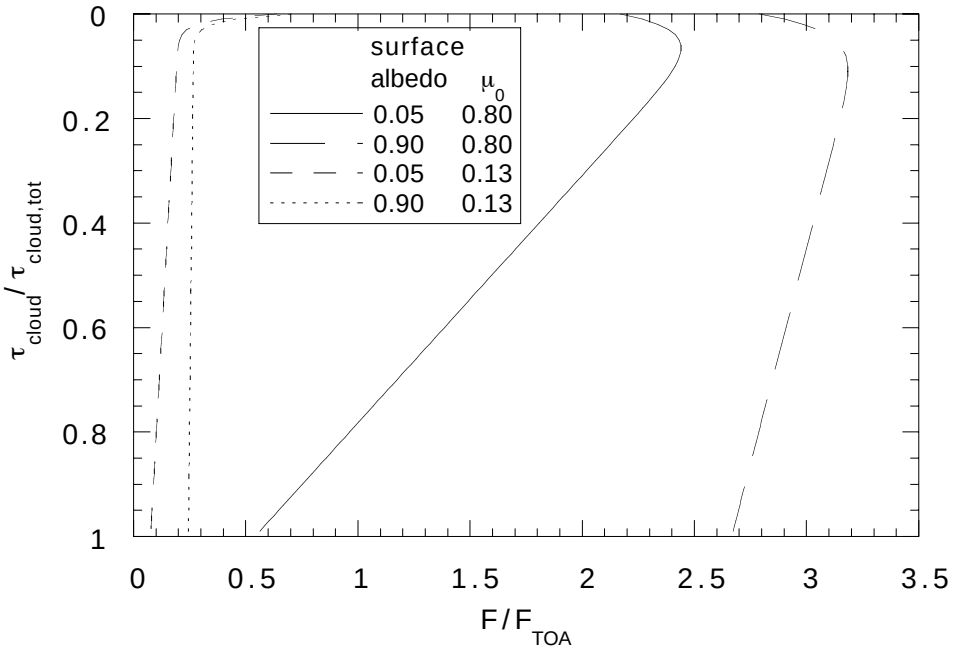

Figure 8. Vertical profiles of the actinic flux in the cloud layer, normalized with the incident actinic flux at the top of the atmosphere, calculated with the delta-Eddington model.